# Laboratory simulations of local winds in the atmospheric boundary layer via image analysis

**Antonio Cenedese[1,*], Marco Giorgilli[1], Monica Moroni[1]**

[1]Department of Civil and Environmental Engineering, Sapienza University of Rome, Rome, Italy
*corresponding author: monica.moroni@uniroma1.it

**Abstract** In the atmospheric boundary layer, under high pressure conditions and negligible geostrophic winds, problems associated with pollution are the most critical. In this situation local winds play a major role in the evaluation of the atmospheric dynamics at small scales and in dispersion processes. These winds originate as a result of non uniform heating of the soil, either when it is homogeneous, or in discontinuous terrain in the presence of sea and/or slopes. Depending on the source of the thermal gradient, local winds are classified into convective boundary layer; sea and land breezes; urban heat islands and slope currents. Local winds have been analyzed by simple analytical models that may capture only some aspects in a qualitative form; numerical models, which being unable to simulate all scales, parameterize turbulence employing empirical or semi-empirical relations; field measurements that are very expensive and provide information only on certain points of the field; laboratory measurements through which it is impossible to completely create the necessary similarities, but the parameters that determine the phenomenon can be controlled and each single wind can be separately analyzed. The present article presents a summary of laboratory simulations of anabatic currents neglecting synoptic winds and the effects of Coriolis force. Image analysis techniques appear suitable to fully describe both the individual phenomenon and its superposition with an urban heat island. Results do agree with other laboratory studies and numerical experiments.
**Keywords:** Local winds, slope flows, laboratory experiments

## 1 Introduction

The movement of air in the atmosphere is governed by the balance of inertia, Coriolis and baroclinic forces, being negligible the effects of viscosity. Near the Earth's surface, which is strongly affected by the change in temperature between day and night (Atmospheric Boundary Layer, ABL), the effects of Coriolis forces are also negligible.
Even when no geostrophic winds occur in the ABL, air movements (hereinafter called local winds [1]) may be generated due to the presence of pressure gradients $\nabla p$ linked to the temperature and density gradients, $\nabla T$ and $\nabla \rho$ respectively, through the state equation of an ideal gas (Figure 1):

$$\frac{\nabla p}{p} = \frac{\nabla T}{T} + \frac{\nabla \rho}{\rho} \tag{1}$$

The fluid behaves baroclinicly, i.e., density is not only a function of pressure but also depends on temperature, resulting in a rotational current with circulation, C, along a line, which can be computed, neglecting viscous effects, from the Bjerknes theorem [2-3]:

$$\frac{DC}{Dt} = \frac{D}{Dt}\oint_{\ell}(\mathbf{u}\cdot\mathbf{s})\,d\ell = -\oint_{\ell}\frac{\nabla p}{\rho}\cdot\mathbf{s}\,d\ell = \int_{S}\frac{\nabla\rho\times\nabla p}{\rho^2}\cdot\mathbf{n}\,dS \tag{2}$$

where:
**u** is the fluid velocity
$\ell$ is the closed line along which C is computed
**s** is the unit vector tangent to $\ell$
S is the surface defined by $\ell$
**n** is the normal at each point of the surface S
The spatial scales that characterize local winds range from the mesoscale $\alpha$ (hundreds of kilometers) to the

microscale δ (millimeters, isotropic turbulence conditions hold) [4]. The corresponding temporal scales range from days to seconds. Therefore, it is extremely challenging to simultaneously account for this variety of orders of magnitude in the investigation of the physical, chemical, biological and geological processes characterized by local winds. With the exception of the larger scales, Coriolis forces are always negligible with respect to advective and viscous/turbulent forces. Rossby (ratio among inertia and Coriolis forces) and Ekman (ratio among viscous/turbulent and Coriolis forces) numbers are therefore large.

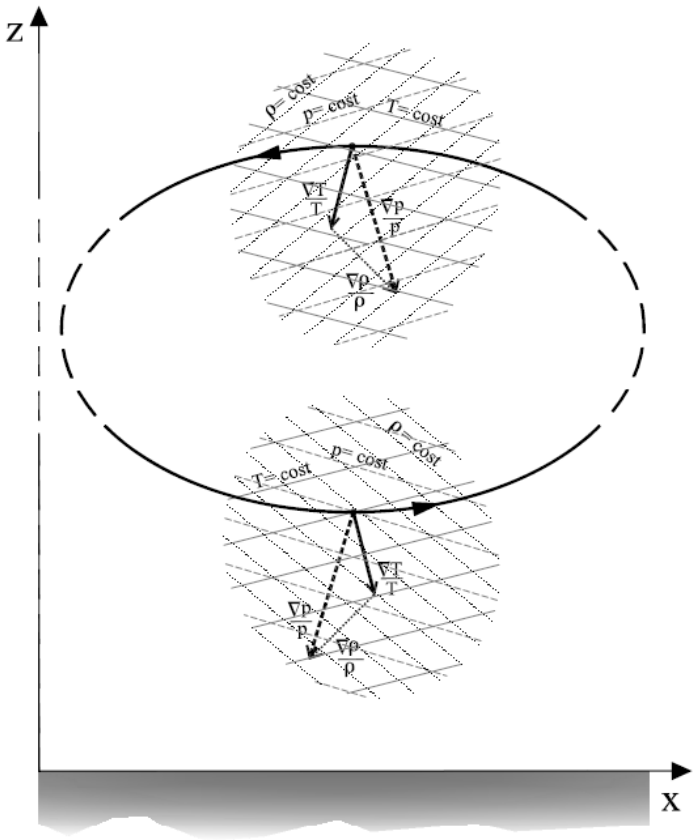


Fig. 1 Flow within a baroclinic fluid

Figure 2 schematizes the daily evolution of the energy budget for some typical situations (desert, wetland, and sea); $R_{NE}$ is net radiation (sum of outgoing terrestrial radiation and incoming solar radiation taking into account the albedo), $Q_{SE}$ sensible heat flux and $Q_{EV}$ evaporative latent heat flux. All quantities often exhibit a strong variation during the course of a day, mostly in response to the diurnal variation of radiative energy input at the surface, and strongly depend on the nature of the land surface.

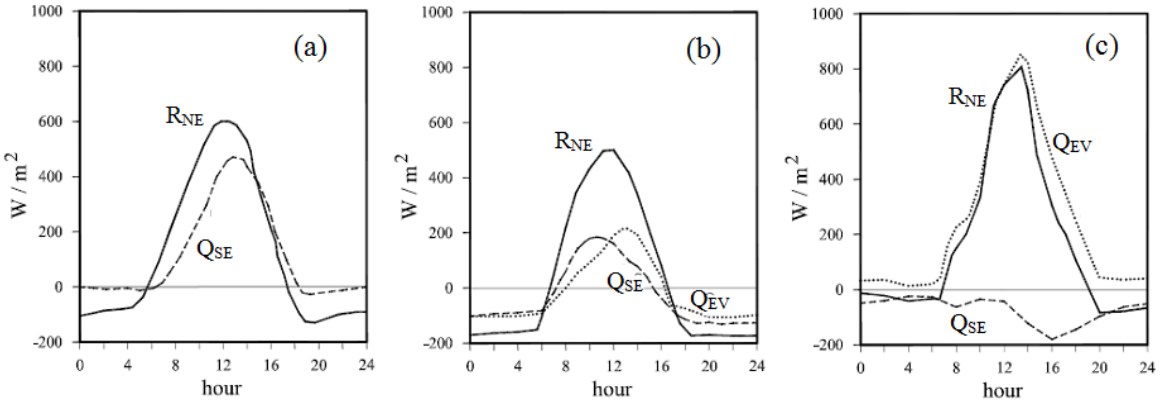


Fig. 2 Daily evolution of the net solar radiation $R_{NE}$, sensible heat $Q_{SE}$ and evaporative latent heat $Q_{EV}$ for a) desert; b) wet soil; c) sea

Depending on the origin of the temperature gradient triggering the air movement, local winds are classified as:

- convective boundary layer;
- sea and land breeze;
- urban heat island;
- slope currents.

Local winds have been studied by analytical modeling [5-6], numerical simulations [7-8], laboratory experiments [9-13] and field surveys [14-15]. None of these can provide completely exhaustive answers. Therefore their combined use appears to be the most appropriate way to characterize such a complex phenomenon.

At the Fluid Mechanics Laboratory of DICEA - Sapienza University of Rome, several laboratory simulations of local winds have been set up, and the analysis of both single phenomena and their interactions has been carried out [16-19]. In this work we present the results of the laboratory simulations of anabatic currents in a closed valley in the presence and the absence of an urban heat island.

## 2 Equations and dimensional analysis

In the investigation of thermal convection, the thermodynamic quantities (density ρ, temperature T, pressure p) are generally decomposed into a constant value, $()_0$, in a term variable along the vertical direction z, $()_a$, and in the deviation from the fluid condition in the absence of motion, $()_m$:

$$\rho(x,y,z,t) = \rho_0 + \rho_a(z) + \rho_m(x,y,z,t) \tag{3}$$

$$T(x,y,z,t) = T_0 + T_a(z) + T_m(x,y,z,t) \tag{4}$$

$$p(x,y,z,t) = p_0 + p_a(z) + p_m(x,y,z,t) \tag{5}$$

The hydrostatic background situation is then described by $()_0+()_a$:

$$\frac{\partial(p_0 + p_a)}{\partial z} = \frac{\partial p_a}{\partial z} = -g(\rho_0 + \rho_a) \tag{6}$$

In the limit:

$$|\rho_0| >> |\rho_a| >> |\rho_m| \tag{7}$$

the Boussinesq hypothesis can be introduced, i.e. the density change in the fluid can be neglected in the fluid dynamic balance equations, except in the gravity term appearing in the momentum equation, where ρ is multiplied by g [20-21]. For a liquid this hypothesis appears evident; for gases the hypothesis can be justified considering that pressure variations are small with respect to the density variations:

$$\left|\frac{p_m}{p_0}\right| << \left|\frac{\rho_m}{\rho_0}\right|; \qquad \left|\frac{p_m}{p_0}\right| << \left|\frac{T_m}{T_0}\right| \tag{8}$$

Then:

$$\frac{\rho_m}{\rho_0} = -\frac{T_m}{T_0} = -\frac{\theta_m}{\theta_0} \tag{9}$$

with θ the potential temperature, decomposed analogously to T.

Assuming the quantities characterising the fluid behaviour (viscosity $\mu$, thermal conductivity $k_T$, constant pressure specific heat $c_p$) are constant, the equations employed to study the atmospheric boundary layer are:

- state equation:

$$\rho = \rho_0\left[1 - \beta(T - T_0) + \gamma(p - p_0)\right] \cong \rho_0\left[1 - \beta(T - T_0)\right] \tag{10}$$

for a perfect gas $\beta = 1/T_0$

- the mass balance equation

$$\frac{\partial u_i}{\partial x_i} = 0 \tag{11}$$

- the momentum balance equation

$$\frac{\partial u_i}{\partial t} + u_j \frac{\partial u_i}{\partial x_j} = -g\frac{\rho_m}{\rho_0}\delta_{i3} - \frac{1}{\rho_0}\frac{\partial p_m}{\partial x_i} + \nu\frac{\partial^2 u_i}{\partial x_j^2} = g\beta T_m\delta_{i3} - \frac{1}{\rho_0}\frac{\partial p_m}{\partial x_i} + \nu\frac{\partial^2 u_i}{\partial x_j^2} \tag{12}$$

- energy balance equation without sources, sinks and radiative sources within the field:

$$\frac{\partial T}{\partial t} + u_j\frac{\partial T}{\partial x_j} = \kappa_T\frac{\partial^2 T}{\partial x_j^2} \tag{13}$$

where $\kappa_T = k_T/\rho_0 c_p$ is the thermal diffusivity. In the limit of validity of the Boussinesq hypothesis, the potential temperature $\theta$ can be used instead of temperature T.

The temperature or the temperature gradient, i.e., the heat flux, may be imposed as boundary conditions. The heat flux at the ground surface per unit area $Q_s$, computed through the Fourier's law, is generally imposed:

$$Q_s = -k_T\frac{\partial T}{\partial z} = \rho_0 c_p q_s = h_q(T_s - T_\infty) = h_q\Delta T \tag{14}$$

where:

- $q_s$ is the kinematic heat flux at the ground surface
- $h_q$ is the heat transport coefficient
- $T_s$ is the temperature at the ground surface
- $T_\infty$ is the temperature immediately outside the thermal boundary layer.

Thermal exchanges may be due to buoyancy (free convection), to the imposed velocity (forced convection) or both (mixed-type convection). Equations may be non-dimensionalised [22-23] in different ways, as a function of the dependent variables to be considered. If $h_q$ is considered a dependent variable, it will be a function of:

- $\rho_0$ reference density
- $\mu$ viscosity
- $c_p$ specific heat at constant pressure
- $k_T$ thermal conductivity
- L reference length
- V reference velocity
- $g\beta\Delta T$ buoyancy force per unit mass

$$h_q = f(\rho_0, \mu, c_p, L, k_T, V, g\beta\Delta T) \tag{15}$$

The following non-dimensional variables, marked with the symbol ()*, can be introduced:

$$x_i^* = x_i / L; \quad u_i^* = u_i / V; \quad t^* = t\,V / L; \quad T^* = \frac{T}{T_s - T_\infty} = \frac{T}{\Delta T}; \quad p^* = \frac{p}{\rho_0 V^2} \tag{16}$$

The momentum equation and the energy equation will then be obtained in a non-dimensional form

$$\frac{\partial u_i^*}{\partial t^*} + u_j^* \frac{\partial u_i^*}{\partial x_j^*} = -\frac{\partial p_m^*}{\partial x_i^*} + \frac{Gr}{Re^2} T_m^* \delta_{i3} + \frac{1}{Re} \frac{\partial^2 u_i^*}{\partial x_j^{*2}} \tag{17}$$

$$\frac{\partial T^*}{\partial t^*} + u_j^* \frac{\partial T^*}{\partial x_j^*} = \frac{1}{RePr} \frac{\partial^2 T^*}{\partial x_j^{*2}} \tag{18}$$

where the following non-dimensional numbers have been introduced:

- Reynolds $Re = \frac{\rho_0 V L}{\mu}$ ratio between advective terms and viscous forces
- Grashof $Gr = \frac{\rho_0^2 g\beta\Delta T L^3}{\mu^2}$ ratio between buoyancy and viscous forces
- Prandtl $Pr = \frac{c_p \mu}{k_T} = \frac{\nu}{\kappa_T}$ ratio between dynamic diffusion and thermal diffusion

According to (15) and Buckingham theorem, the Nusselt number, which represents the non-dimensional heat flux at the surface, is given by:

$$Nu = \frac{h_q L}{k_T} = Nu(Re, Gr, Pr) \tag{19}$$

The three non-dimensional numbers result from the choice of V, $g\beta\Delta T$, $c_p$ as quantities belonging each to a non-dimensional group only. Other choices are possible. Alternatively, other non-dimensional numbers are employed, related to the ones previously introduced:

- Rayleigh $Ra = \frac{\rho_0 g\beta\Delta T L^3}{\mu\kappa_T} = Gr\,Pr$ ratio between buoyancy forces and the damping effect due to the viscosity and the thermal diffusivity
- Peclet $Pe = \frac{\rho_0 V c_p L}{k_T} = Re\,Pr$ ratio between thermal convection and thermal diffusion

If $Gr/Re^2 << 1$, the effects of forced convection prevail and the second term on the right-hand side of equation (17) can be neglected. It is then Nu=Nu(Re, Pr). If $Gr/Re^2 >> 1$, the effects of free convection prevail; in the limit of V=0, the Reynolds number cannot be introduced (Nu=Nu(Gr, Pr)).
The phenomenon of free convection can be considered quasi-stationary if, taking the thermal inversion height as the reference length ($L=z_i$) and introducing the convective velocity as the reference velocity:

$$w_* = (g\beta\Delta T z_i)^{1/2} \tag{20}$$

it is $\partial z_i / \partial t << w_*$. The balance equations in non-dimensional form can be obtained by employing $z_i$ and $w_*$ as reference quantities for length and velocity:

$$\frac{\partial u_i^*}{\partial t^*} + u_j^* \frac{\partial u_i^*}{\partial x_j^*} = -\frac{\partial p_m^*}{\partial x_i^*} + \delta_{i3} T_m^* + \frac{1}{Gr^{1/2}} \frac{\partial^2 u_i^*}{\partial x_j^{*2}} \tag{21}$$

$$\frac{\partial T^*}{\partial t^*} + u_j^* \frac{\partial T^*}{\partial x_j^*} = \frac{1}{Pr\, Gr^{1/2}} \frac{\partial^2 T^*}{\partial x_j^{*2}} \tag{22}$$

Then, Nu=Nu(Gr,Pr). The same result can be achieved if the kinematic heat flux $q_s$ at the ground is used as the independent variable instead of the temperature difference. In this case, the convective velocity is given by:

$$w_* = \left(g\beta q_s z_i\right)^{1/3} \tag{23}$$

If the phenomenon is non-stationary, the evolution of the inversion height must be analyzed and $z_i$ can be considered as a dependent variable:

$$z_i = f(h_q, \rho_0, \mu, c_p, N, k_T, g\beta\Delta T) \tag{24}$$

with:

- $N = \sqrt{g\beta\Gamma}$ Brunt-Väisälä frequency
- $\Gamma = \frac{\partial(\theta_0 + \theta_a)}{\partial z} = \frac{\partial \theta_a}{\partial z}$ potential temperature vertical gradient

The reference quantities are:

- for length $L_* = \left[\mu/(\rho_0 N)\right]^{1/2}$
- for time $t_* = 1/N$
- for velocity $w_* = \left[(\mu N)/\rho_0\right]^{1/2}$

The non-dimensional equations then take the same form as (21) and (22) with:

$$Pr = \frac{\mu c_p}{k_T}; \quad Gr = g\beta\Delta T\left[\rho_0/(\mu N^3)\right]^{1/2}; \quad Nu = \frac{h_q}{k_T}\left(\frac{\mu}{\rho_0 N}\right)^{1/2} \tag{25}$$

If the thermal forcing has a characteristic frequency ω (i.e., the diurnal frequency $\omega=2\pi/(24\cdot3600)$), a fourth non-dimensional number is introduced, i.e. ω/N. To account for the Coriolis force, a further non-dimensional number can be introduced f/N where $f=2\,\omega\sin\varphi$ and φ is the latitude.

When dealing with turbulent phenomena, after decomposing all the dependent quantities within the balance equations into mean and fluctuating components ( $b = \overline{b} + b'$ ), turbulent fluxes appear as: $\overline{u_i' u_j'}$ in the momentum equation and $\overline{u_i' \theta'}$ in the energy balance equation. For those fluxes, a local closure of the first order can be introduced:

$$-\overline{u_i' b'} = K_b \frac{\partial \overline{b}}{\partial x_i} \tag{26}$$

One may assume $K_b$ (eddy viscosity or eddy diffusivity related to quantity b) to be a function of the turbulent kinetic energy per unit mass:

$$\bar{e} = \frac{1}{2}\overline{u_i'^2} = TKE \tag{27}$$

The TKE balance equation for the mean value $\bar{e}$ is:

$$\frac{D\bar{e}}{Dt} = \frac{\partial \bar{e}}{\partial t} + u_j \frac{\partial \bar{e}}{\partial x_j} = P_{tur} + G_{tur} + T_{tur} - D_{tur} \tag{28}$$

- the production term $P_{tur}$ is related to the transfer of energy from the mean flow to the turbulent fluctuations:

$$P_{tur} = -\overline{u_i' u_j'} \frac{\partial \overline{u_i}}{\partial x_j} \tag{29}$$

- the production term $G_{tur}$ expresses the variation of kinetic energy due to buoyancy forces:

$$G_{tur} = \delta_{i3} \beta g \overline{u_i' \theta'} \tag{30}$$

- the transport term $T_{tur}$ can be written in divergence form:

$$T_{tur} = \frac{\partial}{\partial x_j}\left( -\overline{e u_j'} - \frac{1}{\rho_0}\overline{p' u_j'} + \nu \frac{\partial \bar{e}}{\partial x_j} \right) \tag{31}$$

the three terms are responsible for the redistribution of turbulent energy by velocity fluctuations, pressure fluctuations and viscosity respectively; the last term playing a role only close to solid boundaries;

- the dissipation term $D_{tur}$ is given by:

$$D_{tur} = \frac{\nu}{2}\overline{\left( \frac{\partial u_i'}{\partial x_j} + \frac{\partial u_j'}{\partial x_i} \right)^2} \tag{32}$$

A solution for equation (28) can be obtained if a closure for $\overline{e u_j'}$ is assumed. Neglecting viscous dissipation, which is important only close to the wall, and since terms of divergence-type ($\partial \overline{u_j' e} / \partial x_j$, $\partial \overline{u_j' p} / \partial x_j$) are responsible for energy transfers within the flow field, global variations of TKE are determined by buoyancy terms, $\delta_{i3} \beta g \overline{u_i' \theta'}$, and shear terms, $-\overline{u_i u_j}\left(\partial \overline{u_i} / \partial x_j\right)$, the latter term being always positive meaning that the energy is always transferred from the mean to the turbulent motion.
The Richardson number is introduced to characterize the stability conditions. It is the ratio of the term related to the kinematic heat flux and the term related to the kinematic momentum flux. If the hypothesis of horizontal homogeneity holds ($\partial \bullet / \partial x << \partial \bullet / \partial z; \partial \bullet / \partial y << \partial \bullet / \partial z$) and winds of prevalent horizontal direction are assumed ($\overline{w} << \sqrt{\overline{u}^2 + \overline{v}^2}$), the "flux" Richardson number is defined as:

$$Ri_f = \frac{\beta \overline{w'\theta'} g}{\left( \overline{u'w'} \frac{\partial \overline{u}}{\partial z} + \overline{v'w'} \frac{\partial \overline{v}}{\partial z} \right)} \tag{33}$$

Taking into account (26) which relates turbulent correlations to mean quantity gradients, the "gradient" Richardson number can be obtained:

$$Ri_g = \frac{g\beta \frac{\partial \overline{\theta}_a}{\partial z}}{\left[\left(\frac{\partial \overline{u}}{\partial z}\right)^2 + \left(\frac{\partial \overline{v}}{\partial z}\right)^2\right]} = \frac{N^2}{\left[\left(\frac{\partial \overline{u}}{\partial z}\right)^2 + \left(\frac{\partial \overline{v}}{\partial z}\right)^2\right]} \tag{34}$$

Taking into account the maximum variations of the variables in the field ($\Delta\bullet$), the "bulk" Richardson number is obtained:

$$Ri_b = g\beta\Delta z \frac{\Delta\overline{\theta}}{(\Delta\overline{u})^2 + (\Delta\overline{v})^2} = \frac{N^2\Delta z^2}{(\Delta\overline{u})^2 + (\Delta\overline{v})^2} \tag{35}$$

## 3 Experimental setup

Experiments are conducted in a rectangular tank (Figure 3) with a length of 1.700 m, a height of 0.210 m and a width of 0.600 m that is open at the top and has a horizontal aluminum surface at the bottom. Two flat 0.146 m long (along the x-axis) and 0.320 m wide (along the z-axis) flat aluminium plates, simulating the slope, are mounted above the bottom surface one opposite to the other to form a valley. The plate inclination angle is set to $\alpha$= 20°. Distilled water is used as working fluid, to allow both a large heating rate and sufficient time to take measurements of the evolving thermal structures. To allow optical access, the lateral sides of the tank are made up of 0.010 m thick transparent glass. The temperature $\theta_s$ of the bottom surface is controlled by a heat exchanger connected to a heating bath circulator, while the temperature $\theta_u$ of the upper surface is set by means of a second heat exchanger. By doing so, a nearly linear vertical stratification profile of the needed intensity ($\Gamma$), reached after about 16 hours, simulates a stably stratified potential temperature distribution. A polystyrene sheet is placed over the top of the tank to reduce heat losses. The temperature of the sidewalls is not controlled, but it could be reasonably considered constant during the experiments.
Heating during the daytime and radiative cooling during the nighttime experienced by the slope surface are simulated by means of a series of Peltier cells solidal to the inclined plate. The Peltier cell is a small thermoelectric solid state device that can operate as a heat pump utilizing the Peltier effect. When connected to a power source, the current causes heat to move from one side of the cell to the other, creating a hot side and a cold side on the cell. If the current is reversed, the heat moves in the opposite direction. In other words, the hot face becomes the cold face and vice versa. Therefore, the slope is cooled or warmed up when the upper side of the cell is the cold or the hot face, respectively. A problem may arise, however, since the cooling and warming of the bottom face results in undesired temperature changes in the surroundings. To avoid this problem, the bottom face of the plate is embedded in an enclosure built beneath the aluminum plate within which forced water at constant temperature minimized the temperature oscillations of the bottom face of the plate. For the simulation of the katabatic flow, a downward (negative) heat flux $Q_{slope}$ was considered while for the anabatic flows the heat flux was upward (positive). During the experiments aimed at investigating the anabatic currents, the test section bottom surface was heated to initiate and sustain convection.
In the case of interaction of the anabatic current and an UHI, the surplus of surface heat flux $Q_{UHI}$ between the city and its rural environment is simulated by means of a thin (~0.2 mm), rectangular-shaped electric heater 0.300 m long and 0.050 m wide connected to a suitable power supply. Note that, because of the geometry of the heater, in the absence of other circulations, the flow associated with the simulated UHI is expected to be nearly two-dimensional planar.
Information about flow kinematics is achieved by using a software package based on particle-tracking, namely Feature Tracking (FT) [24], a non-intrusive technique developed for tracking non-buoyant particles (pine pollen, $\sim 80\,\mu m$ in diameter assuming the same density as the seeded liquid [24]) Temperatures were measured using 27 T-Type thermocouples mounted on three rakes (9 thermocouples per rake) placed at representative locations in the flow (A, B, C; Figure 3). The thermocouples were equally spaced every 0.004

m in the vertical direction from 0 to 0.032 m. A further array of 23 thermocouples, covering the entire water depth, was used for measuring the initial temperature distribution. Disturbances in the velocity field produced by the racks of temperature sensors were minimized by positioning the racks in a plane parallel to the one illuminated by the light source, placed at a distance of nearly 0.050 m.
Assume two 2D reference systems lying in the vertical plane passing through the center of the inclined plates simulating the slopes: 1) (s-n), where s is positive downslope and n is the coordinate normal to it (positive upward), and 2) (x-z) with a horizontal, x, and vertical, z, axis centered in the middle of the heater location. The monitored area is rectangular, lying in the vertical plane passing through the center of the slope. Figure 4 presents the reference systems and locations of detected temperature and velocity profiles.
Table 1 presents the values of characteristic quantities varied in the two experiments presented here.

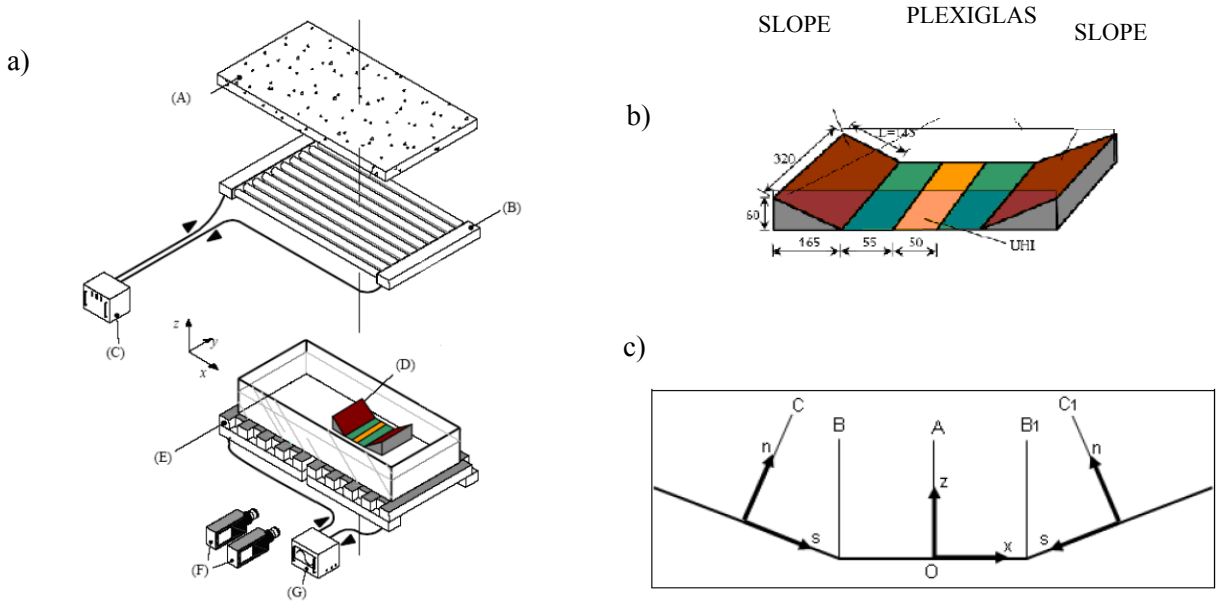


Fig. 3 a) Experimental apparatus: (A) polystyrene sheet, (B) Free surface heat exchanger, (C) Free surface thermostat, (D) Valley model, (E) Bottom surface heat exchanger, (F) Cameras, (G) Bottom surface thermostat. b) Valley model with two slopes (units are in mm). c) Reference systems and locations of temperature arrays velocity profiles

| **Experiment** | Experiment description | $\theta_s$ (K) | $\theta_u$ (K) | $\Gamma$ (K/m) | $Q_{slope}$ (kW/m²) | $Q_{UHI}$ (kW/m²) |
|---|---|---|---|---|---|---|
| 1 | Anabatic flow | 302 | 314 | 100 | 1.5 | - |
| 2 | Anabatic flow – UHI interaction | 302 | 314 | 100 | 1.5 | 0.6 |

Table 1. Experiment parameters.

## 4 Flow field in a fluid measured through image analysis techniques

The need for measuring velocity fields has historically led researchers to develop experimental techniques and related instrumentation. An 'ideal' measurement system should be non intrusive to avoid flow field perturbations, should not require calibration, and should be suitable for obtaining the velocity field with a time and space resolution smaller than the characteristic time and length scales (i.e. Kolmogorov scale for turbulent flows). Velocity measurements based on optical methods capable of providing the velocity of tracer particles illuminated by a light source represent the best approximation of this 'ideal' system.
Most of today's velocity measurements are performed with either single point-based techniques (i.e. Laser Doppler anemometry (LDA), Hot Wire Anemometry) or multi-point-based global measurements in a plane (i.e. Particle Image Velocimetry (PIV), Particle Tracking Velocimetry (PTV), Feature Tracking (FT)) or even throughout an object volume (3D-PIV, 3D-PTV).
The velocity measurements based on optical methods require the working fluid to be seeded with neutrally

buoyant particles which are assumed to follow the flow. The velocity vector is evaluated from the ratio of the tracer displacement, Äs, and the time interval Ät required for the displacement to take place:

$$\mathbf{u} = \frac{\Delta \mathbf{s}}{\Delta t} \tag{36}$$

The time interval must be small enough for the approximation to be reasonable. The development of more and more advanced high-resolution techniques now allows measurements of time intervals less than 1 μs and distances less than 1 μm, providing information for characterization of flow behavior at its smallest time and spatial scales. Single-point based techniques are characterized by a fixed Äs (distance between the interferential fringes in the volume individuated by the intersection of two laser rays in LDA) and the measured Ät. Multi-point measurement techniques require the measurement of Äs, whereas the acquisition time interval Ät is fixed.
The main limitations associated with these techniques are related to both the need for an experimental apparatus with transparent walls in order to allow optical access, and the need for tracer particles to seed the working fluid. The presence of particles inside the fluid implicitly introduces bias errors. What is really measured in these frameworks are the tracers velocities. The difference between the fluid velocity and the measured particle velocity is a function of the local fluid acceleration, of the particles size, of the difference between fluid and tracers densities; the difference grows with these quantities.
The techniques allowing simultaneous multi-point velocity measurements in a plane (2D measurement techniques) will be described next. PIV evaluates the average displacement of particles belonging to a sub-region (interrogation area) of the whole imaged area using correlation between couple of images [25]. PIV reconstructs the Eulerian velocity field on a regular, equi-spaced grid. PTV includes all the methods in which the displacements of every single particle are considered to reconstruct trajectories [16]. Velocity is then evaluated from a Lagrangian point of view considering the ratio between particle displacement along the reconstructed trajectories and the correspondent time interval. PTV provides sparse velocity vectors at points coincident with particle centroid positions. Feature Tracking (FT), belonging to particle tracking techniques, reconstructs the displacement field by selecting image features (image portions suitable to be tracked because their luminosity remains almost unchanged for small time intervals, likely located along tracer particle boundaries) and tracking these from frame to frame. The matching measure used to follow a feature (and its interrogation window) and its "most similar" region at the successive times is the "Sum of Squared Differences" (SSD) among intensity values: the displacement is defined as the one that minimizes the SSD. In Feature Tracking one applies the algorithm only to points where the solution for the displacement exists: those points are called "good features to track" [24, 26].
The Lagrangian description is particularly suitable to study dispersion phenomena. The transition from one description to another is always possible. While shifting from the Lagrangian to the Eulerian description implies an integration, which allows the use of a low pass filter to reduce noise, the transition from the Eulerian to the Lagrangian description requires the solution of a system of differential equations that amplifies noise.
PTV is usually less extensively used but, compared to PIV, allows a larger spatial resolution (being able to detect regions very close to the walls) and an increased dynamic range. On the other hand, since seeding must be very sparse to ensure successful tracking, important features in turbulent flow may not be resolved even though each successful velocity measurement is highly localized. Both PIV and FT use interrogation windows, PIV identifies the highest peak within the correlation matrix and FT solves a minimization problem. PTV and FT in particular compared to PIV allows a larger spatial resolution (being able to detect regions closer to the box boundaries) and an increased dynamic range. Further, providing trajectories instead of velocity field, it allows understanding and qualitatively detecting flow characteristics much easier than PIV. Compared to other tracking algorithms, FT allows one to ignore the constraint of low seeding density, being able to provide accurate displacement vectors even when the number of tracer particles within each image is very large.
The main steps for characterising the velocity field of an anabatic current via image analysis are reported below.

- Image acquisition with a high resolution CMOS camera (1732×2532 pixels) at 10 Hz of time resolution; the framed area is 0.023×0.007 m² (Figure 4).

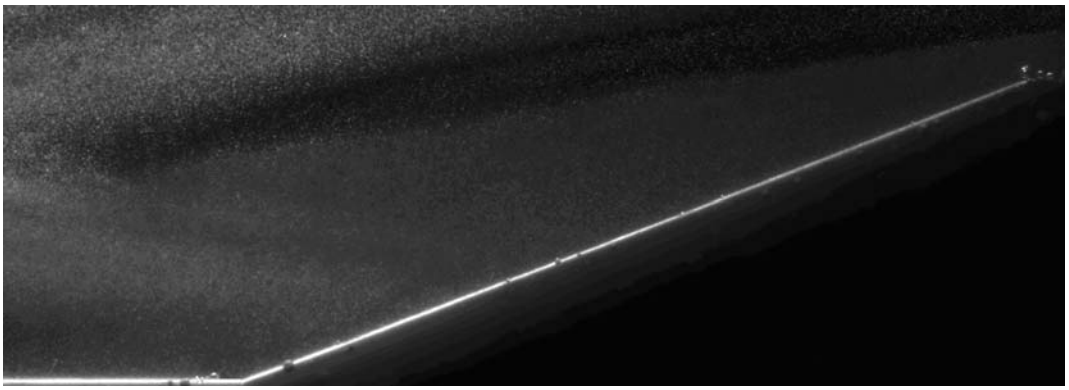

Fig. 4 Sample image acquired during a slope flow experiment with a high resolution camera (4 Mpixels)

- Noise attenuation and elimination of boundaries and areas with no particles.
- Recognition of a particle and the coordinates of its centroid (Figure 5).
  An ideal particle detection routine should satisfy the following requirements:
  - detect images of isolated particles;
  - detect superimposed images or clusters of particles and be able to split them;
  - detect other features of the image, such as glare, background noise or scene objects and remove them with confidence;
  - assess the quality of the image in terms of noise level, particle diameter and shape and predict the accuracy to which real particles can be located.

  The particle detection algorithm used to analyze the images acquired during the experiments reported herein is based on image thresholding (based on the image gray scale histogram) and labeling of lighted pixels. Once image pixels have been classified through thresholding in a background and foreground set, the image has to be analyzed to find all the possible particle candidates and evaluate the geometrical characteristics useful for their validation. This procedure is called labeling and involves marking each foreground pixel with a label that identifies which particle image candidate the pixel belongs to. The output of this process consists of sets of labeled pixels. All the pixels with the same label are identified as one single particle image candidate. The centroid coordinates are computed as the average of the pixel locations weighted by their grey levels. When FT is employed, the position of particles is analogously determined considering the grey levels in the proximity of feature individuated. The set of validated particle image locations is finally used as input data for the tracking algorithm. More than 7000 particles have been detected per image.
- Particle tracking and Lagrangian description of the flow field (Figure 6).
  Various tracking techniques have been developed to identify successive positions of the same particle and thus extract the displacement and velocity of that particle along its trajectory. The tracking procedure consists of building a circle of fixed radius centered at a centroid location and looking for a centroid in the successive time within the circle. This condition is equivalent to assuming a maximum velocity in the investigated flow. To add spots to the two-point trajectories the nearest neighbor principle ("minimum acceleration" criterion) within a circle of fixed radius is employed.
- Reconstruction of the Eulerian flow field on a regular grid of 92×38 knots; five sparse velocity samples per knots were available on average; velocity data were further averaged over time intervals of 1 seconds (10 frames) (Figure 7).
  Post-processing and presentation of experimental data are extremely important in representing and understanding flow behavior. Moreover, the post-processing method ultimately determines the accuracy of the information extracted from the velocity vectors. The interpolation step is necessary to map randomly spaced fields onto regular grids, to replace erroneous vectors with values computed from the neighboring vectors or to refine the original grid. The interpolation step, due to the low-pass filtering process, determines the loss of the high frequency flow features.

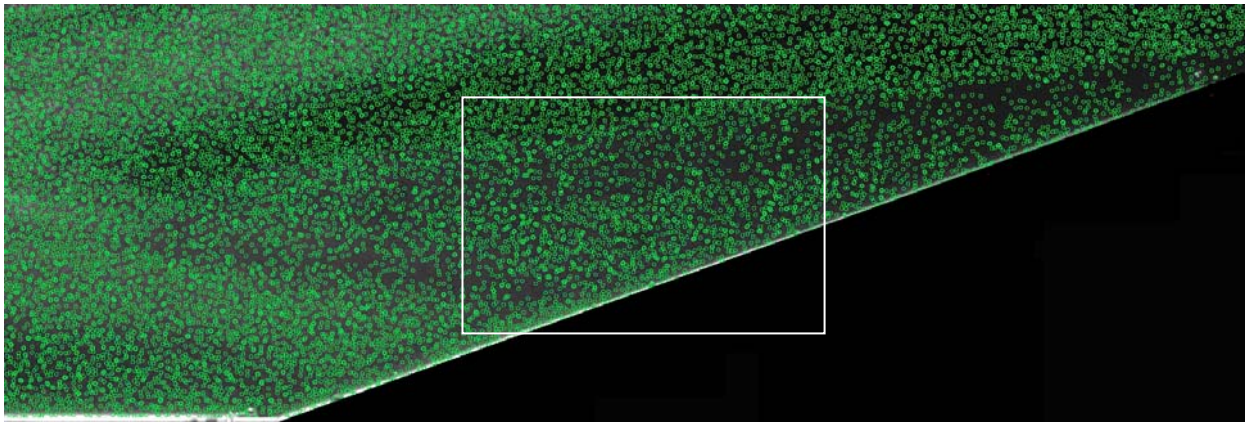

(a)

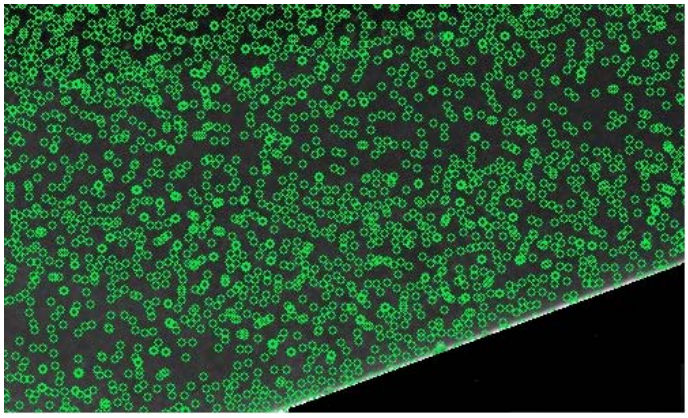

(b)

Fig. 5 Particle centroids reconstructed by FT: (a) whole image and (b) zoom in the area highlighted

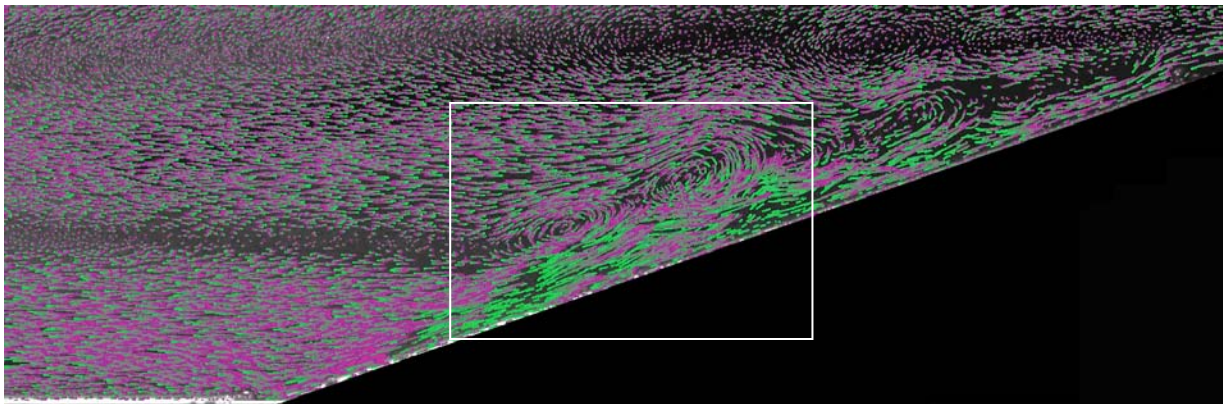

(a)

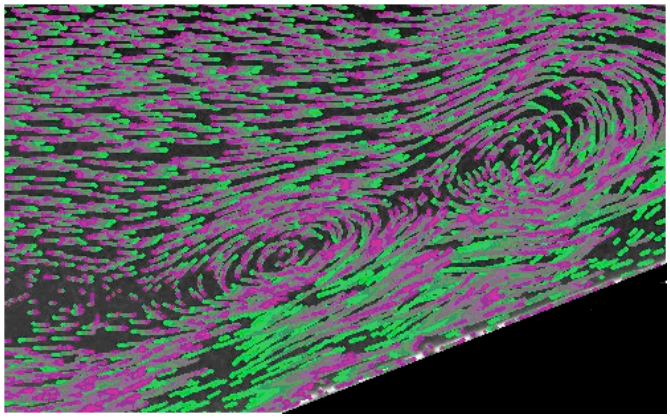

(b)

Fig. 6 Trajectories reconstructed by FT: (a) whole image and (b) zoom in the area highlighted

- Evaluation of vorticity (Figure 8).
  The velocity field obtained by image analysis technique frequently is an intermediate result in the investigation of complex flow phenomena. Further post-processing is required to extract important fluid mechanical properties. For validation of numerical tools and for aerodynamic studies, a precise knowledge of the vortical flow is desired. The vorticity field may be obtained from the velocity gradient. As a finite difference from noisy velocity data, the vorticity field may present an augmented noisy level which can in turn adversely influence the determination of the vortex centers. The squared vorticity field or enstrophy further enhances the visibility of the vortices but it is equally susceptible to noise.
- Streamlines reconstruction (Figure 9).
  The analysis of streamlines provides a topological description of fluid-dynamic field highlighting the presence of critical points: nodes, saddles and foci.

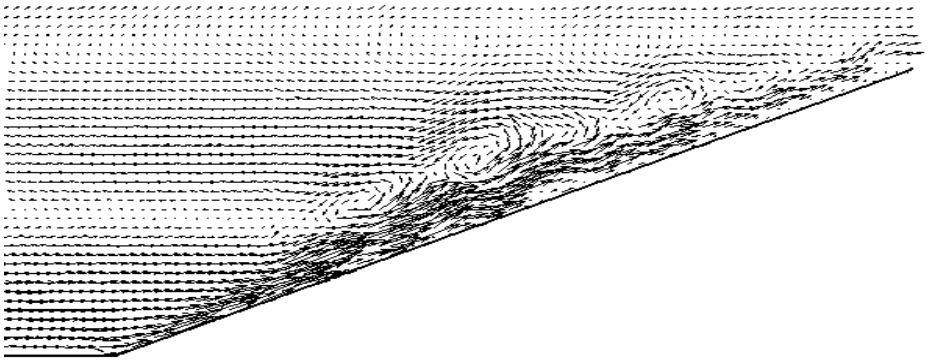

Fig. 7 Eulerian velocity fields

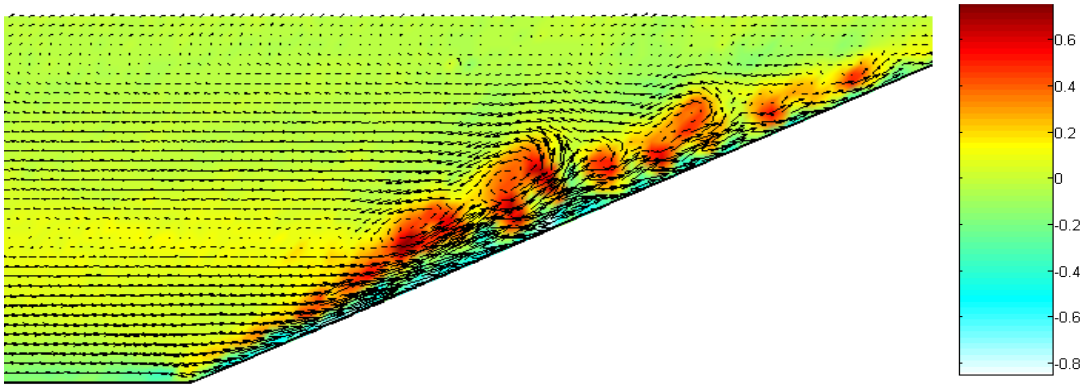


Fig. 8 Vorticity map

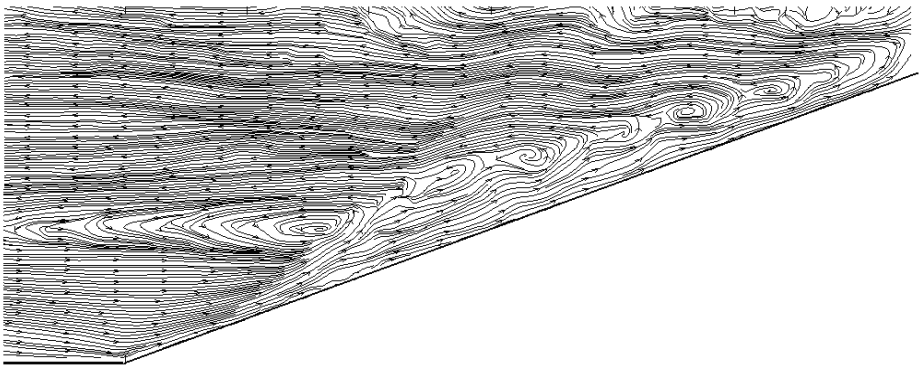

Fig. 9 Streamlines

## 5 Anabatic current

The results of the simulation of a 2D anabatic current will be presented. In the fluid, a thermal stratification of 100 K/m was obtained by setting the bottom and the top fluid temperatures at 302 K and 314 K respectively. Once a stable stratification was obtained, to simulate the diurnal heating, the Peltier cells along the slopes have been heated producing a heat flux of 1.5 kW/m$^2$. Simultaneously, the bottom temperature was increased of 4 K. The time origin is set at the beginning of the heating.
Although there was the attempt to reproduce a symmetrical situation, with respect to the vertical plane passing through the center of the valley, temperature and velocity fields present asymmetries which, although detectable, do not alter the qualitative and quantitative interpretation of the phenomenon [27].
In Figure 10, the velocity and vorticity fields reported in an Eulerian form have been obtained by averaging over intervals of 1 s (10 frames).

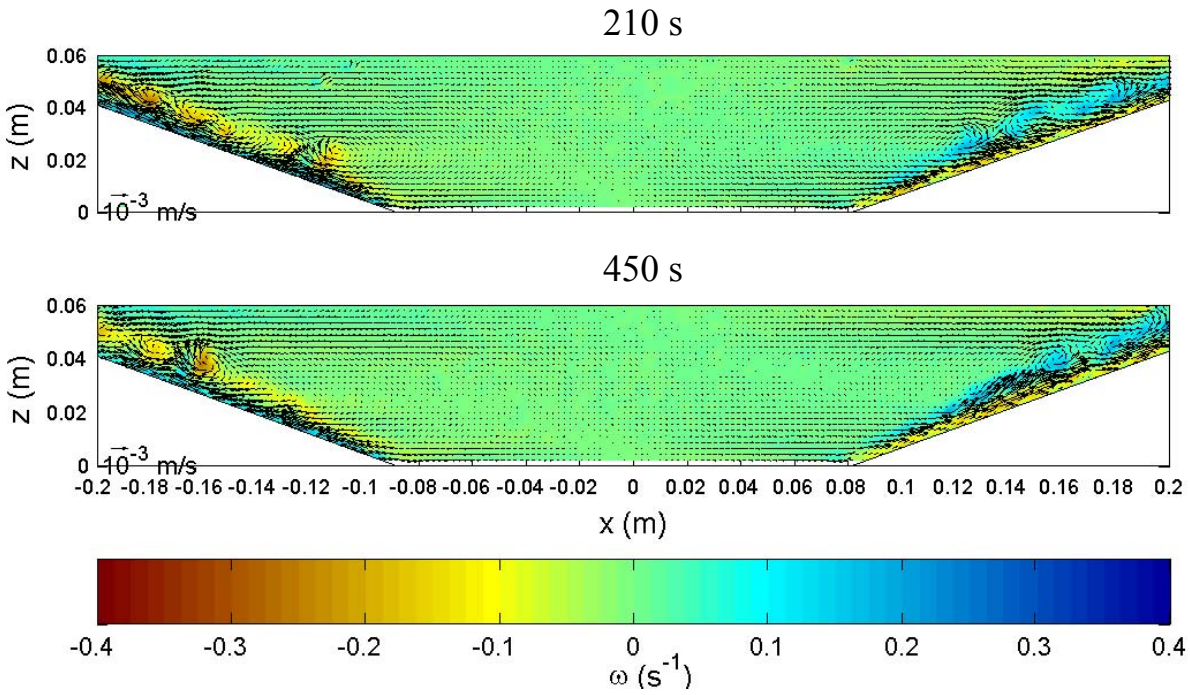


Fig. 10 Velocity and vorticity fields at t=210 s and t=450 s for case 1, Γ=1 K cm$^{-1}$, average over 1 s

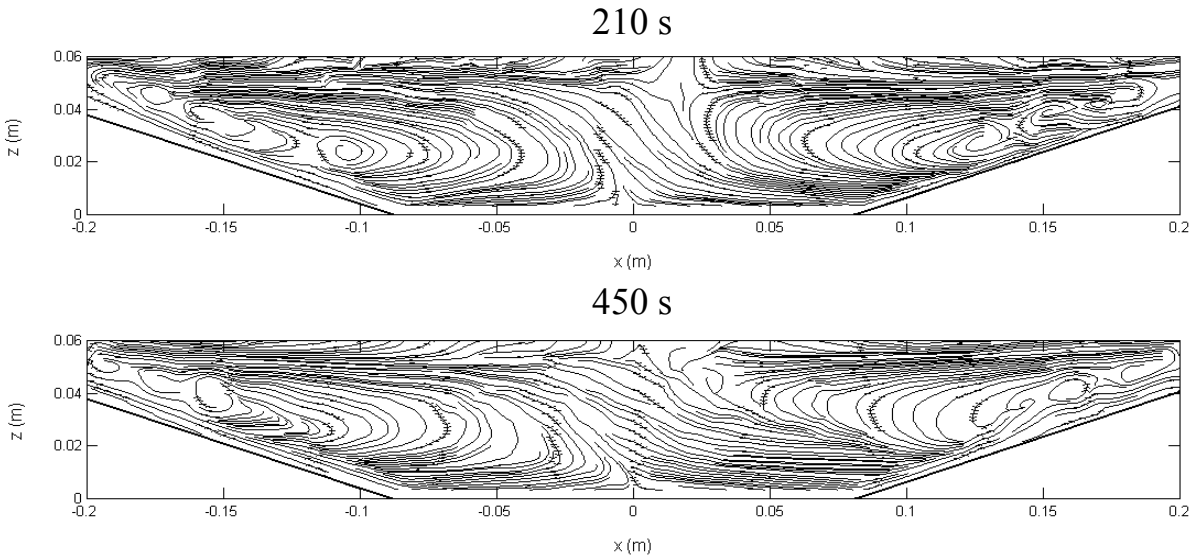


Fig. 11 Streamlines obtained processing the velocity fields reported in Figure 10 at times t=210 s and t=450 s

The anabatic current manifests itself through the presence of vortices moving upslope. From the top of the slope, the circulation closes with return currents toward the center of the valley and a weak downdraft at the center [28]. This behavior is clearly shown by streamlines reported in Figure 11. These aspects are highlighted by the velocity profiles obtained by averaging over 10 seconds (100 frames) in different time instants (Figure 12).

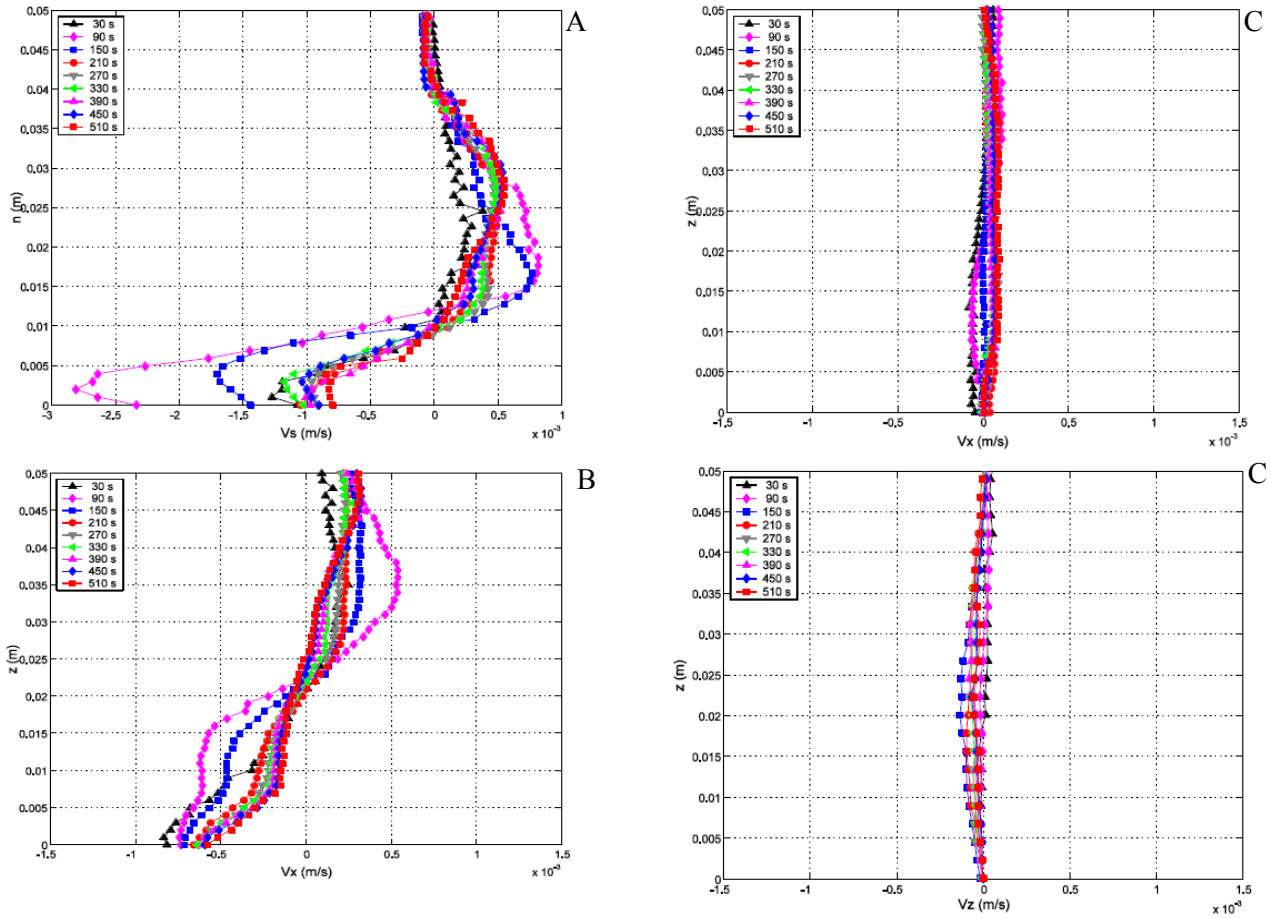


Fig. 12 Velocity profiles in different sections for case 1 (for the profile location refer to Figure 3c)

## 6 Interaction between anabatic current with and an urban heat island

The interaction between an anabatic current and an urban heat island was investigated on the same initial thermal stratification. The UHI was simulated through an additional heat flux of $Q_{UHI}$=0.6 kW/m$^2$ provided by the electric heater placed in the center of the valley. Such a heat flux was triggered 30 s before heating the slope and the bottom.

Figures 13 and 14 present the velocity fields and streamlines obtained by averaging over 1 s (10 frames). In this case, four cells are formed, two of which extend over half of the valley and involve the anabatic currents, the return currents and the consequent subsidence motion in the central area. The other two cells are the symmetrical convective cells that represent the circulation associated to urban heat island. A further current originated at the slope top and moving toward the slope foot can be observed.

A more complex behaviour than the one described for the anabatic current can be observed from the velocity profiles at different locations and for different times (Figure 15).

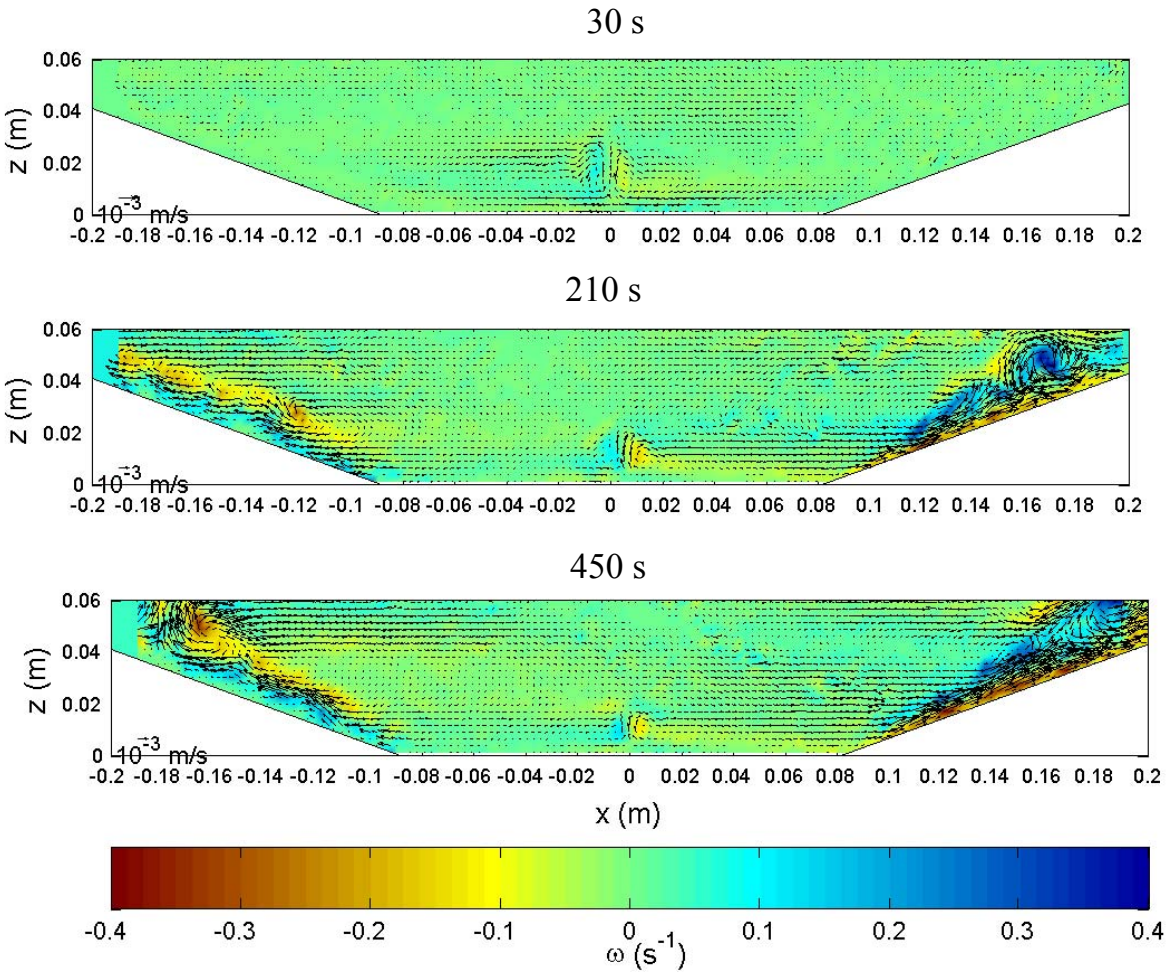


Fig. 13 Velocity and vorticity fields at t=30 s, t=210 s and t=450 s for case 2, Γ=1 K cm$^{-1}$, average over 1 s

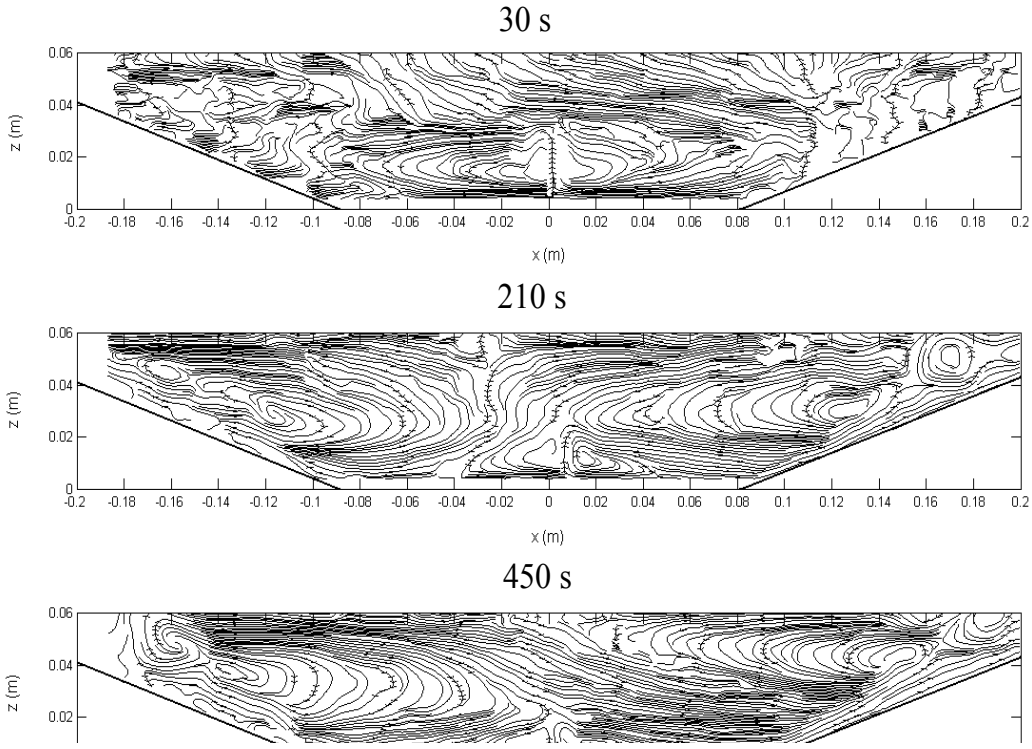


Fig. 14 Streamlines obtained processing the velocity fields reported in Figure 13 at times t=30 s, t=210 s and t=450 s

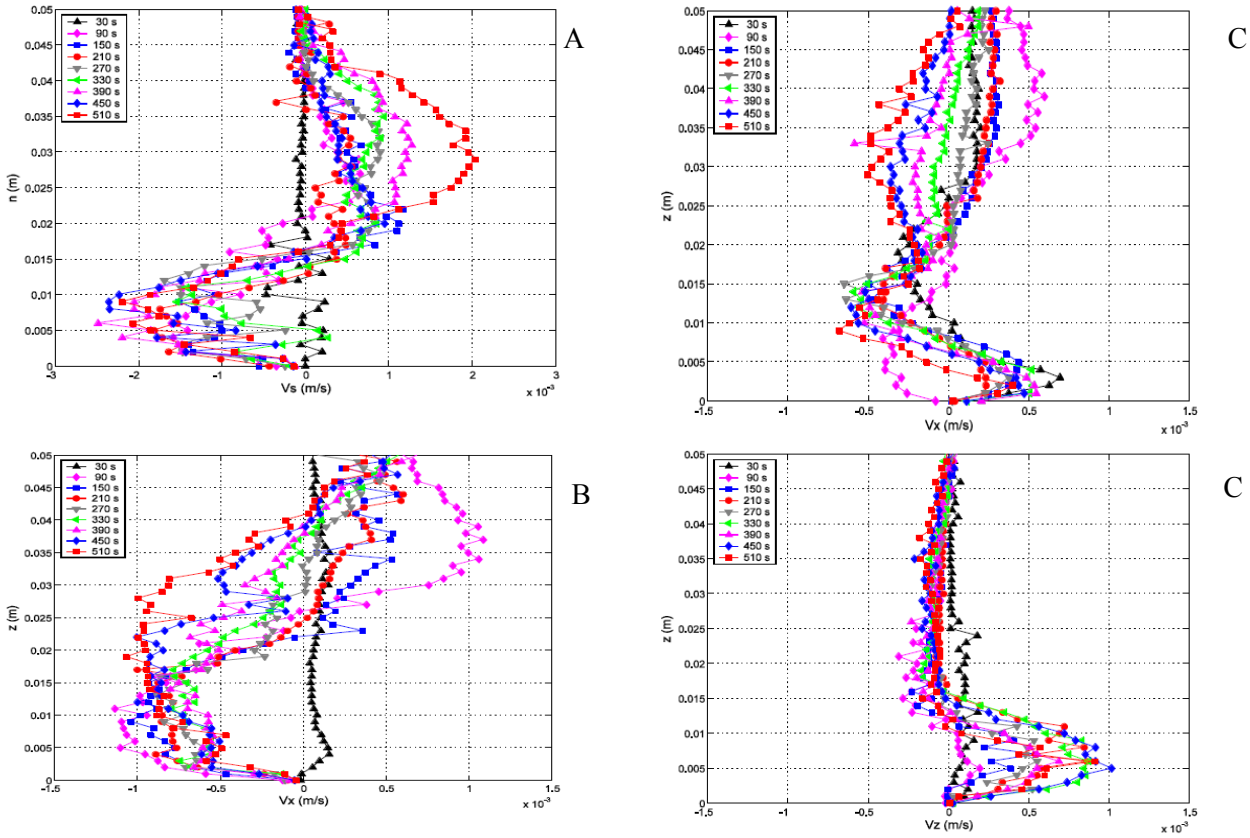


Fig. 15 Velocity profiles in different sections for case 2 (for the profile location refer to Figure 3c)

In those profiles, in addition to the upslope and return currents, an upward current in the valley center (close to the bottom), due to the UHI, and a weak downward current at higher heights, due to the anabatic current recirculation, can be observed.

## 7 Conclusions

Though in laboratory simulations it is impossible to reproduce Reynolds (if it can be defined), Rayleigh and Grashof numbers that characterize geophysical flows at a real scale, useful information can be gathered to better understand the origin and evolution of complex phenomena, such those related to the presence of local winds.

In real scale investigations, it is very difficult, if not impossible, to isolate the single typologies of circulations. In laboratory, through the proper control of initial and boundary conditions, it is possible to highlight both separately and jointly the effects of the different motion forcings.

As highlighted, techniques based on image analysis provide a proper description of the flow under investigation allowing to evidence also the smaller spatial and temporal scales.

## References

[1] Simpson J E (1994) Sea breeze and local winds. Cambridge University Press.

[2] Gill A E (1982) Atmosphere-ocean dynamics. Academic Press (London).

[3] Pedlosky J (1979) Geophysical Fluid Dynamics. Springer Verlag.

[4] Stull R B (1999) Meteorology for Scientists and Engineers. Cengage Learning.

[5] Manins P C, Sawford B L (1979) A Model of Katabatic Winds. *J. Atmos. Sci.*, 36, 619-630.

[6] Hunt J C R, Fernando H J S, Princevac M (2003) Unsteady Thermally Driven Flows on Gentle Slopes. *J. Atmos. Sci.*, 60, 2169-2182.

[7] Moeng C H, Dudhia J, Klemp J, Sullivan P (2007) Examining two-way grid nesting for large eddy simulation of the PBL using the WRF model. *Mon. Wea. Rev.*, 135, 2295-2311.

[8] Nieuwstadt F T M, Mason P J, Moeng C H, Schumann U (1992) Large-eddy Simulation of the Convective Boundary Layer: A Comparison of Four Computer Codes. Turbulent Shear Flows 8. Springer.

[9] Hibberd M F, Sawford B L (1994) A saline laboratory model of the Planetary Convective Boundary layer. *Boundary-Layer Meteorol.*, 67, 229-250.

[10] Willis G E, Deardorff J W (1987) Buoyant Plume Dispersion and Inversion Entrapment In and Above a Laboratory Mixed Layer. *Atmos. Environ.*, 21, 1725-1735.

[11] Lu J, Arya S P, Snyder W H, Lawson Jr. R E (1997a) A laboratory study of the urban heat island in a calm and stably stratified environment. Part I: Temperature field. *J. Appl. Meteor.*, 36, 1377–1391.

[12] Lu J, Arya S P, Snyder W H, Lawson Jr. R E (1997b) A laboratory study of the urban heat island in a calm and stably stratified environment. Part II: Velocity field. *J. Appl. Meteor.*, 36, 1392–1402.

[13] Moroni M, Cenedese A (2015) Laboratory Simulations of Local Winds in the Atmospheric Boundary Layer via Image Analysis. *Advances in Meteorology*, 618903.

[14] Fedorovich E, Kaiser R (1997) Wind tunnel model study of turbulence regime in the convective atmospheric boundary layer. Boundary Convection in Geophysical Flows (Plate et al. eds). Kluwer Academic Publishers.

[15] Salizzoni P, Grosjean N, Méjean P, Perkins RJ, Soulhac L, Vanliefferinge R (2007) Wind Tunnel Study of the Exchange Between a Street Canyon and the External Flow. Air Pollution Modeling and Its Application XVII.

[16] Cenedese A, Querzoli G (1997) Lagrangian statistics and transilient matrix measurements by PTV in a convective boundary layer. *Meas. Sci. Technol.*, 8, 1553-1561.

[17] Cenedese A, Monti P (2003) Interaction between an Inland Urban Heat Island and a Sea Breeze Flow: a Laboratory Study. *J. Appl. Meteor.*, 42(11), 1569-1583.

[18] Cenedese A, Monti P (2004) The Proper Orthogonal Decomposition in the Analysis of a Laboratory Simulation of Land- and Sea-Breeze Regimes. *J. Fluid Mech.*, 510, 1-28.

[19] Dore V, Moroni M, Le Menach M, Cenedese A (2009) Investigation of penetrative convection in stratified fluids through 3D-PTV. *Exp. Fluids*, 47(4-5), 811-825.

[20] Spiegel E A, Veronis G (1960) On the Boussinesq approximation for a compressible fluid. *Astrophysical Journal*, 131, 442-447.

[21] Gray D D, Giorgini G (1976) The validity of the Boussinesq approximation for liquids and gases. *Int. J. Heat Mass Transfer*, 19, 545-551.

[22] Hanke G (2008) An Introduction to Fluid Mechanics and Transport Phenomena. Springer.

[23] Baremblatt G (2003) Scaling. Cambridge Univ Pr.

[24] Moroni M, Cenedese A (2005) Comparison among feature tracking and more consolidated velocimetry image analysis techniques in a fully developed turbulent channel flow. *Meas. Sci. Technol.*, 16, 2307-2322.

[25] Adrian R J (1991) Particle-imaging techniques for experimental fluid mechanics. *Annu. Rev. Fluid Mech.*, 23, 261-304.

[26] Shi J, Tomasi C (1994) Good features to track. IEEE Conference on Computer Vision and Pattern Recognition (CVPR94), Seattle.

[27] Shindler L, Giorgilli M, Moroni M, Cenedese A (2013) Investigation of local winds in a close valley: an

experimental insight using Lagrangian particle tracking. *Journal of Wind Engineering & Industrial Aerodynamics*, 114, 1-11.

[28] Moroni M, Giorgilli M, Cenedese A (2014) Experimental investigation of slope flows via image analysis techniques. *Journal of Atmospheric and Solar-Terrestrial Physics*, 108, 17-33.